

This document is the Accepted Manuscript version of a Published Work that appeared in final form in Nano Letter, copyright © American Chemical Society after peer review and technical editing by the publisher. To access the final edited and published work see <https://doi.org/10.1021/acs.nanolett.9b02137>.

Defect Engineering of Palladium-Tin Nanowires Enables Efficient Electrocatalysts for Fuel Cell Reactions

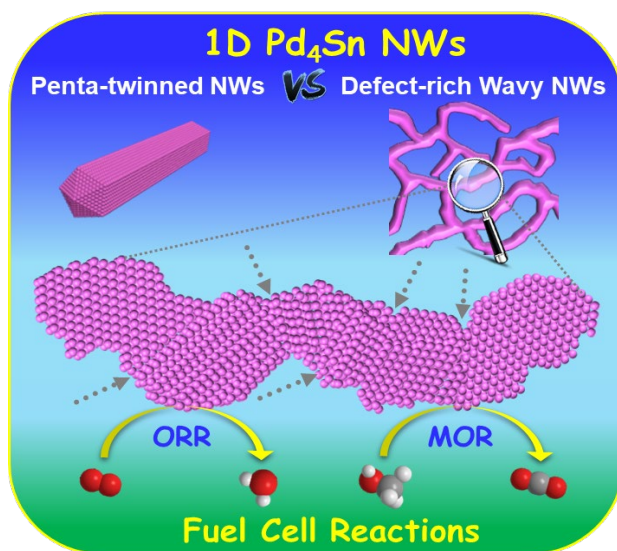
Ying Zhang,[†] Bolong Huang,[‡] Qi Shao,[†] Yonggang Feng,[†] Likun Xiong,[§] Yang Peng,[§] and Xiaoqing Huang^{*†}

[†]College of Chemistry, Chemical Engineering and Materials Science, Soochow University, Jiangsu, 215123, China.

[‡]Department of Applied Biology and Chemical Technology, The Hong Kong Polytechnic University, Hung Hom, Kowloon, Hong Kong SAR, China.

[§]Soochow Institute for Energy and Materials Innovations, Soochow University, Jiangsu 215006, China.

E-mail: hxq006@suda.edu.cn



Abstract: The defect engineering of noble metal nanostructures is of vital importance because it can provide additional yet advanced tier for further boosting catalysis, especially for one-dimensional (1D) noble metal nanostructures with high surface to bulk ratio and more importantly the ability to engineer the

defect along the longitudinal direction of the 1D nanostructures. Herein, for the first time, we report that the defect in 1D noble metal nanostructures is a largely unrevealed yet essential factor in achieving highly active and stable electrocatalysts towards fuel cell reactions. The detailed electrocatalytic results show that the Pd-Sn nanowires (NWs) exhibit interesting defect-dependent performance, in which the defect-rich Pd₄Sn wavy NWs display the highest activity and durability for both methanol oxidation reaction (MOR) and oxygen reduction reaction (ORR). Density functional theory (DFT) calculations reveal that, a large amount of surface vacancies/agglomerated voids are the driving forces of forming surface grain boundaries (GBs) within Pd₄Sn WNWs. These electronic active GB regions are the key factors of preserving amounts of Pd⁰-sites, which are critical for minimizing the intrinsic site-to-site electron-transfer barriers. Through this defect engineering, the Pd₄Sn WNWs ultimately yield highly efficient alkaline ORR and MOR. The present work highlights the importance of defect engineering in boosting the performance of electrocatalysts for potentially practical fuel cells and energy applications.

Keywords: Defect Engineering, Pd-Sn, Nanowire, Oxygen Reduction Reaction, Electrocatalysis

The development of high-performance nanocatalysts is an eternal theme in chemical conversions, sensors, fuel cells, *etc.*¹⁻⁶ which is of vital for developing green renewable energy towards energy infrastructure revolution and hazard emission reduction. Noble metal nanocatalysts play a central role in these applications due to their efficient and unique catalytic properties.⁷⁻¹¹ It is generally recognized that the catalytic behavior of noble metal nanocatalysts is highly dependent on their structures.¹²⁻¹⁸ To this end, the control of noble metal nanocatalysts has been deeply explored through various strategies over the past decades, by which many issues, such as sizes, morphologies, compositions and phases, have been extensively evaluated.¹⁹⁻²² In fact, the properties of noble metal nanocatalysts can also be deeply affected

by the defect, while the related demonstrations are still rare and far from the trial.

The microscopic structure of nanocrystals, particularly the defects referring to the position where the structural integrity of the crystal is destroyed, can be classified as point defect (vacancy, interstitial atom), line defect (dislocation, dislocation row) and surface defect (grain boundary, stacking fault), and can exhibit unusual chemical reactivity and play important roles in boosting catalysis performance due to their defect-modulated surface electronic structure.²³⁻³⁰ For example, Ling and co-workers reported that the O-vacancies on the {111}-O facets favorably affected the electronic structure of single-crystal CoO nanorods, resulting in the enhanced charge transfer and optimal energetics for both oxygen reduction reaction (ORR) and oxygen evolution reaction.³¹ Li and co-workers demonstrated that the carbon nanotube-graphene complexes possessed high ORR electrocatalytic activity and durability owing to the formation of abundant edges and defect sites in outer walls.³² In spite of these well-known demonstrations,³¹⁻³³ the defect effects on noble metal nanocatalysts are still largely unexplored to date. A key challenge in decoding the defect effects on metal catalysis is that the extreme difficulties in creating metal nanocatalysts with controllable defects that can be used for precisely exploiting the correlation between defects and the catalytic properties. It is expected that the generated metal nanostructures with a high density of defects allow for the creation of highly active catalysts. Typically, one-dimensional (1D) nanostructures are ideal nanostructures owing to their high aspect ratio and the important ability to engineer crystal defect along the longitudinal direction of NWs.³⁴ Therefore, achieving fine defect control in 1D nanostructures would lead to the successful creation of high-performance nanocatalysts for energy applications.

Herein, we report an effective synthetic strategy for the selectively defect engineered 1D Pd-Sn NWs for highly efficient fuel cell electrocatalysts. Defect-rich Pd₄Sn wavy nanowires (WNWs) and Pd₄Sn NWs with penta-twinned nanostructures were successfully prepared by simply changing the reaction solvent.

More significantly, we demonstrate that the defects in 1D Pd-Sn NWs largely boost the overall performance in electrocatalysis. Especially, the defect-rich Pd₄Sn WNWs show excellent activity and long durability in both cathodic ORR and anodic MOR electrocatalysts relative to penta-twinned Pd₄Sn NWs as well as commercial Pd/C and Pt/C. Density functional theory (DFT) calculations show that the surface defected region exhibits high electronic activities for charge-transfer and structural flexibility in weakening the over-binding effect, which is the key for boosting the ORR performance.

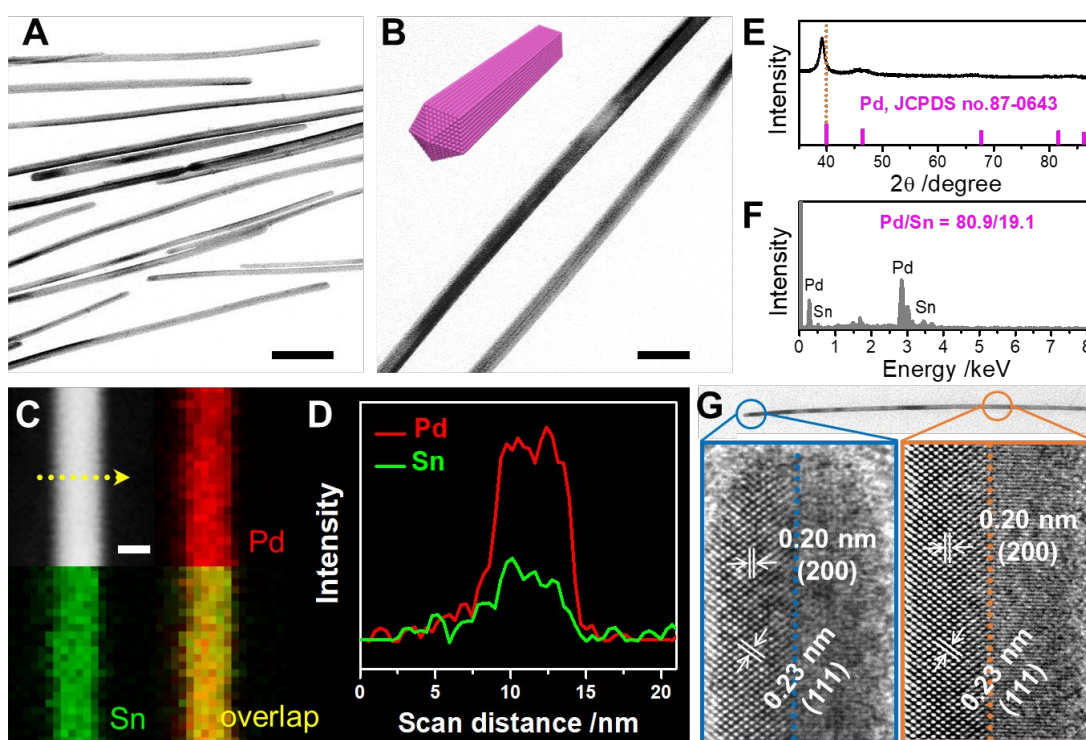


Figure 1. (A, B) TEM images, (C) HAADF-STEM image and corresponding elemental mapping images of Pd₄Sn NWs with red for Pd and green for Sn. (D) Line-scan analysis across the yellow arrow in the (C). (E) PXRD pattern, (F) SEM-EDS spectrum and (G) HRTEM images of Pd₄Sn NWs. Inset in (B) shows a structural model of Pd₄Sn NW. The scale bars in a, inset of (A), (B) and (C) are 50, 20 and 5 nm, respectively.

The 1D Pd-Sn nanostructure was typically prepared by a facile method in the presence of Pd(acac)₂ and Sn(Ac)₂, PVP, NH₄Br, and DMAC/EG (see the Supporting Information for details). The synthesis of

Pd₄Sn WNWs was similar to that of Pd₄Sn NWs by simply changing the solvent (DMAC) with the mixed solvent (DMAC and EG). Transmission electron microscopy (TEM) images of the Pd₄Sn NWs are shown in **Figure 1A** and **1B**. It is found that the NWs with smooth surface exhibit high aspect ratio with the length of hundreds of nanometers and the average diameter of 8 nm. The elemental mapping images and line-scan analysis of Pd₄Sn NWs are also presented (**Figure 1C** and **1D**), where Pd and Sn are highly even throughout the NWs. As shown by the powder X-ray diffraction (PXRD) pattern (**Figure 1E**), the diffraction peaks of Pd₄Sn NWs shift to low-angle region compared with the metallic Pd diffractions (JCPDS card no. 87-0643), suggesting that the incorporation of Sn into face-center-cubic (*fcc*) Pd results in the formation of alloyed Pd-Sn nanomaterials.³⁵ The atomic ratio of Pd to Sn is ~ 4: 1, as confirmed by scanning electron microscopy energy-dispersive X-ray spectroscopy (SEM-EDS) (**Figure 1F**), closing to the feeding amounts of Pd and Sn. The high-resolution TEM (HRTEM) images taken from the end and middle section of individual Pd₄Sn NW reveal the existence of twin boundary with two sets of lattice fringes with the spacings of 0.20 nm and 0.23 nm corresponding to the (200) and (111) planes of *fcc* Pd-Sn alloy, respectively (**Figure 1G** and **S1**). The typical selected-area-electron diffraction (SAED) pattern of an individual Pd₄Sn NW was further investigated (**Figure S2**), which could be assigned to two sets of diffraction patterns corresponding to the [001] and [211] zone axis, confirming the existence of twinned planes in Pd₄Sn NWs. The Pd₄Sn NWs possess a penta-twinned characteristic bounded by five (100) facets along sides and ten (111) facets at two ends, which is a common feature among 1D metal nanostructures.³⁶⁻
³⁸ Therefore, the penta-twinned NWs belong to line defect because of the dislocation, in which the central part of the NWs has the highest concentration of defects, and the surface of the penta-twinned NWs has limited defects (**Figure S3**).

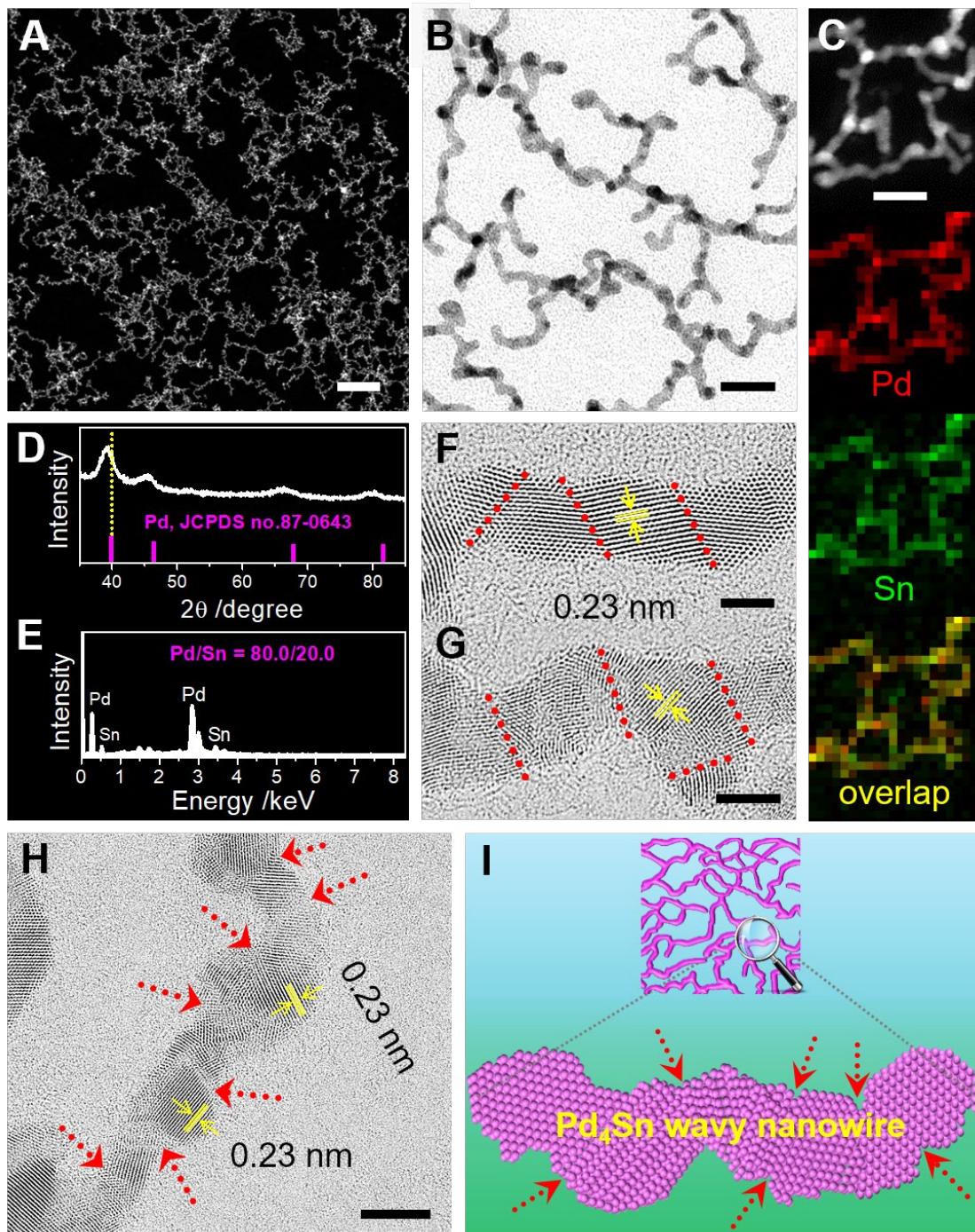


Figure 2. (A) HAADF-STEM image, (B) TEM image, (C) Corresponding elemental mapping images with red for Pd and green for Sn, respectively. (D) PXRD pattern and (E) SEM-EDS spectrum of Pd₄Sn WNWs. (F-H) Cs-corrected TEM images of Pd₄Sn WNWs. Dotted lines in (F) and (G) highlight the presence of twin defects cross-sectioning the WNW. Dashed arrows in (H) highlight the presence of distinct defects/grain boundaries. (I) The structural schematic diagram of the Pd₄Sn WNWs. The scale bars in (A), (B), (C, H) and (F, G) are 200, 20, 5 and 2 nm, respectively.

Interestingly, by simply changing the solvent (DMAC) with the mixed solvent (DMAC and EG), a new type of Pd₄Sn NWs with wavy-like feature (denoted as Pd₄Sn WNWs) were obtained. The morphologies of the Pd₄Sn WNWs were initially determined by high-angle annular dark-field scanning TEM (HAADF-STEM) and TEM images (**Figure 2A** and **2B**). It is evident that the wavy-like NWs are the dominant products with the yield approaching 100 %. The WNWs have high aspect ratios and the diameter as thin as ~3.5 nm. The elemental mapping images of Pd₄Sn WNWs were also represented (**Figure 2C**), where Pd and Sn are uniformly distributed throughout the WNWs. The PXRD of Pd₄Sn WNWs displays similar diffraction peaks of the Pd₄Sn NWs, which can be indexed to Pd-Sn alloy (**Figure 2D**). SEM-EDS spectrum shows that the Pd/Sn composition is 80.0/20.0 (**Figure 2E**). To further evaluate the structure of Pd₄Sn WNWs, the high-resolution spherical aberration correction TEM (Cs-corrected TEM) was carried out. As shown in **Figure 2F-H**, the majority of displayed facets show lattice fringes with the interplanar spacing of 0.23 nm, consistent with the (111) plane of Pd-Sn alloy. In particular, twin defects cross-sectioning the WNWs are obviously observed at the grain boundaries, as pointed by the dotted lines (**Figure 2F, 2G** and **S4**). The Cs-corrected TEM images show that the lattice fringes are discontinuous, and their directions change, mainly because of the wavy morphology of the WNWs. Surface defects are clearly observed near the crystal domain of WNWs, as shown by the red arrows (**Figure 2H**). Therefore, as the schematic shown (**Figure 2I**), the Pd₄Sn WNWs possess a high density of structural defects/grain boundaries (surface defect), which will play a significant role in determining their ultimate catalytic performance.

To better understand the growth mechanism, the reaction intermediates obtained at different reaction times were systematically characterized. As illustrated by TEM images of Pd₄Sn WNWs (**Figure S5**), only uneven nanoparticles were produced at the early stage (15 min), while agglomerations were come

out at 20 min. Short Pd₄Sn WNWs were subsequently found at 30 min and further increased at 45 min with the Pd/Sn ratio of ~ 4:1. After 60 min, Pd₄Sn WNWs with high aspect ratios were obtained. Most likely, this growth pattern was prone to form the discontinuous lattice, thereby creating a large number of lattice defects and grain boundaries. As the reaction time goes on, the diffraction peaks constantly shift to low angle with the increase of Sn content (**Figure S5G**), demonstrating the successful introduction of Sn with large atomic radius into the Pd lattice. The growth process of Pd₄Sn NWs is shown in **Figure S6**. Very fine NWs were formed at the early stage (15 min). As the reaction prolonged to 45 min and up to 60 min, the NWs underwent a process involving inter-diffusion and then transformed into uniform nanostructure with smooth surface. Unlike Pd₄Sn NWs, Pd₄Sn WNWs are formed by the aggregation of nanoparticles with increasing the time. Consequently, the different defect densities on the 1D nanostructures are attributed to the completely different growth patterns.

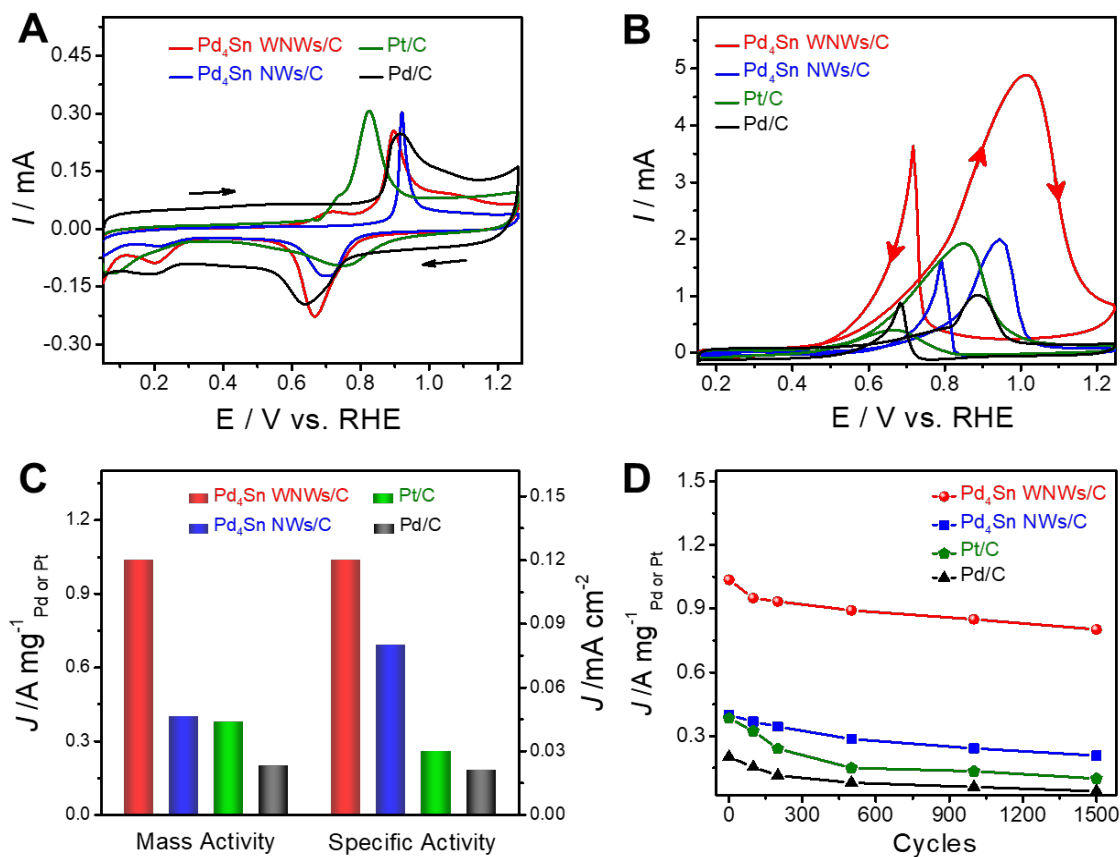


Figure 3. (A) CO-stripping measurements of different catalysts in 0.1 M HClO₄ solution at the scan rate of 20 mV/s. (B) CVs of different catalysts in 0.1 M KOH and 0.5 M methanol solution with a sweep rate of 50 mV/s. (C) Histogram of mass and specific activities of different catalysts for MOR. (D) The changes of electrooxidation peak current densities on different catalysts during cycles.

The prepared Pd₄Sn WNWs and Pd₄Sn NWs with the same component and 1D nanostructures are ideal for investigating whether the defect densities can potentially boost catalytic performance. The unique 1D Pd-Sn nanostructures loaded onto the commercial carbon black (C, Vulcan XC-72R) were initially estimated as anodic electrocatalysts for methanol oxidation reaction (MOR) (**Figure S7**). To measure the electrochemically active surface areas of each catalyst, CO stripping was tested at a sweep rate of 20 mV s⁻¹ in 0.1 M HClO₄ solution. **Figure 3A** shows CO stripping of Pd₄Sn WNWs/C, Pd₄Sn NWs/C, commercial Pt/C and Pd/C (**Figure S8**). The ECSAs of corresponding catalysts were calculated to be 43.0,

26.7, 62.5 and 47.1 $\text{m}^2 \text{g}^{-1}$, respectively (**Figure S9**). Among these catalysts, the ECSA of Pd₄Sn WNWs/C is obviously higher than that of the Pd₄Sn NWs/C, even close to that of commercial Pd/C. To evaluate the performance of 1D Pd-Sn nanostructures, MOR measurements were performed in 0.1 M KOH solution containing 0.5 M methanol solution at a sweep rate of 50 mV s^{-1} . **Figure 3B** compares the CVs of these different catalysts for MOR. The mass and specific activities of all the catalysts are presented in **Figure 3C**. It can be observed that the Pd₄Sn WNWs/C shows the highest mass activity of 1.04 $\text{A mg}_{\text{Pd}}^{-1}$ and specific activity of 0.12 mA cm^{-2} . The mass activity of the Pd₄Sn WNWs/C is 2.7 and 5.2 times higher than those of commercial Pt/C and Pd/C. Especially, even though they are all 1D structures, the mass/specific activities of the Pd₄Sn WNWs/C are 2.6/1.5 times higher than those of Pd₄Sn NWs/C, respectively. The durability of Pd₄Sn WNWs/C, Pd₄Sn NWs/C, Pt/C, and Pd/C for MOR are shown in **Figure 3D**, where all the different catalysts were carried out by cycling the CVs. After 1500 sweeping cycles, 22.6% activity decay is observed for Pd₄Sn WNWs/C, which is much less than those of Pd₄Sn NWs/C (48.0%), Pt/C (74.0%), and Pd/C (80.2%) (**Figure S10**), showing the enhanced MOR durability of the Pd₄Sn WNWs/C. All these data indicate that the MOR performance of the defect-rich Pd₄Sn WNWs/C is obviously superior to that of the Pd₄Sn NWs/C.

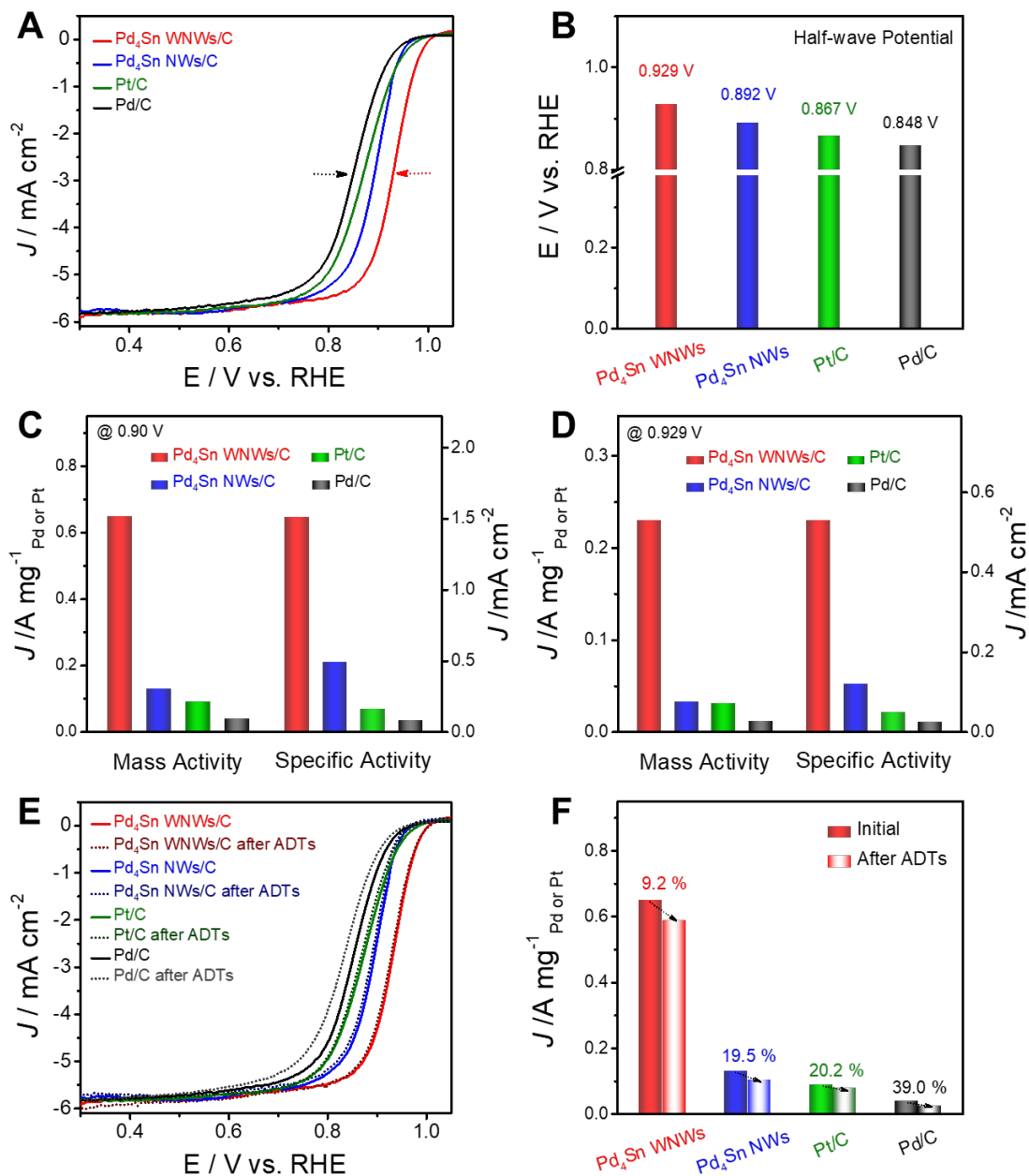


Figure 4. (A) ORR polarization curves, (B) the half-wave potential and ORR mass activities and specific activities of different catalysts at (C) 0.90 V and (D) 0.929 V versus RHE. The ORR polarization curves were recorded at room temperature in an O_2 -saturated 0.1 M KOH aqueous solution at a sweep rate of 10 mV/s and a rotation rate of 1600 rpm. (E) ORR polarization curves and (F) histograms of mass activities for different catalysts before and after 10000 cycles of ADTs.

Encouraged by the enhanced performance of the $\text{Pd}_4\text{Sn WNWs/C}$ for anodic MOR, we further

explored the defect effect on the cathodic ORR performances. The commercial Pt/C and commercial Pd/C were also adopted as references for comparisons. **Figure 4A** shows the ORR polarization curves of the different electrocatalysts carried out in an oxygen (O_2)-saturated 0.1 M KOH solution at a sweep rate of 10 mV s^{-1} and at a rotation rate of 1600 rpm by using the rotating disk electrode (RDE), which were normalized by the area of the glassy carbon area (0.196 cm^2). As shown in **Figure 4B**, the half-wave potential for the Pd₄Sn WNWs/C was 0.929 V versus RHE, which is considerably higher than those of the Pd₄Sn NWs/C (0.892 V), commercial Pt/C (0.867 V) and Pd/C (0.848 V), suggesting relatively high ORR activity of the Pd₄Sn WNWs/C. The kinetic currents at 0.90 V versus RHE were normalized to the Pd (or Pt) loading and ECSA to evaluate the mass and specific activities, respectively (**Figure 4C**). The Pd₄Sn WNWs/C has the highest mass activity of $0.65 \text{ A mg}_{\text{Pd}}^{-1}$ at 0.90 V versus RHE among all the catalysts evaluated, which is 5-fold, 7.2-fold and 16.3-fold higher than those of the Pd₄Sn NWs/C ($0.13 \text{ A mg}_{\text{Pd}}^{-1}$), Pt/C ($0.09 \text{ A mg}_{\text{Pd}}^{-1}$) and Pd/C ($0.04 \text{ A mg}_{\text{Pd}}^{-1}$), respectively. The Pd₄Sn WNWs/C also exhibits a high specific activity of 1.51 mA cm^{-2} , which is 3.0-fold, 9.4-fold and 18.8-fold higher than those of the Pd₄Sn NWs/C (0.49 mA cm^{-2}), commercial Pt/C (0.16 mA cm^{-2}) and Pd/C (0.08 mA cm^{-2}), respectively. We also compared mass and specific activities of different catalysts at the half-wave potential of 0.929 V (**Figure 4D**). Remarkably, the Pd₄Sn WNWs/C still exhibits 7 times higher mass activity and 4.4 times higher specific activity than that of Pd₄Sn NWs/C. From the above results, it is noteworthy that the ORR mass/specific activities of Pd₄Sn WNWs/C are much higher than those of Pd₄Sn NWs/C, further confirming that defect-rich Pd₄Sn WNWs/C can boost fuel cell reactions.

The ORR durability of Pd₄Sn WNWs/C was also examined through CV cycling in a range of 0.4-1.0 V (versus RHE) in 0.1 M KOH at a scan rate of 100 mV s^{-1} . There is almost no shift in ORR polarization curve for Pd₄Sn WNWs/C after 10000-cycle accelerated durability tests (ADTs) (**Figure 4E**). However, under the same test conditions Pd₄Sn NWs/C, Pt/C and Pd/C show obvious negative shifts in ORR

polarization curves. As shown in **Figure 4F**, only 9.2 % mass activity loss is observed for Pd₄Sn WNWs/C with limited morphology and composition changes (**Figure S11A-C**). For comparison, obvious morphology changes of Pd₄Sn NWs/C (19.5% mass activity loss) were observed due to the obvious dissolution of Sn after 10000-cycle ADTs (**Figure S11D-F**). The commercial Pt/C (20.2% loss of mass activity) and Pd/C (39.0% loss of mass activity) also underwent serious aggregation after ADTs tests (**Figure S12**). All these data indicate that the defect-rich Pd₄Sn WNWs/C exhibits not only higher ORR activity, but also enhanced ORR durability.

Considering the distinct catalytic activity of 1D Pd-Sn nanostructures, X-ray photoelectron spectroscopy (XPS) studies were initially conducted to decode their electronic structures. As shown in **Figure S13**, the Pd 3d spectra of Pd₄Sn WNWs/C show two peaks that can be assigned to the Pd 3d_{5/2} and Pd 3d_{3/2} states, and can be further split into two doublets, associated with Pd⁰ and Pd²⁺, respectively. Similarly, the Sn 3d_{5/2} and Sn 3d_{3/2} can be split into two doublets, associated with Sn⁰ and Sn^{x+}, respectively. The atomic ratios of Pd and Sn, derived from the areas of Pd 3d and Sn 3d peaks of 1D Pd-Sn nanostructures, are summarized in **Table S1**. Compared with Pd₄Sn NWs/C, a slight shift (~ 0.13 eV) of Pd 3d_{5/2} peak to lower value is observed, and a higher content of Pd⁰ and Sn^{x+} was revealed in Pd₄Sn WNWs/C. The change of the electronic structure and high content of Pd⁰ and Sn^{x+} are likely associated with the abundant surface defects in Pd₄Sn WNWs, where more free Pd sites and Sn-O bonds would provide more opportunities for adsorption, activation and dissociation of small molecules to enhance catalytic performance. Interestingly, even after ORR and MOR durability tests, the Sn^{x+} component of Pd₄Sn WNWs/C can be mostly maintained, which makes the activity being retained to a large extent (**Figure S13**).

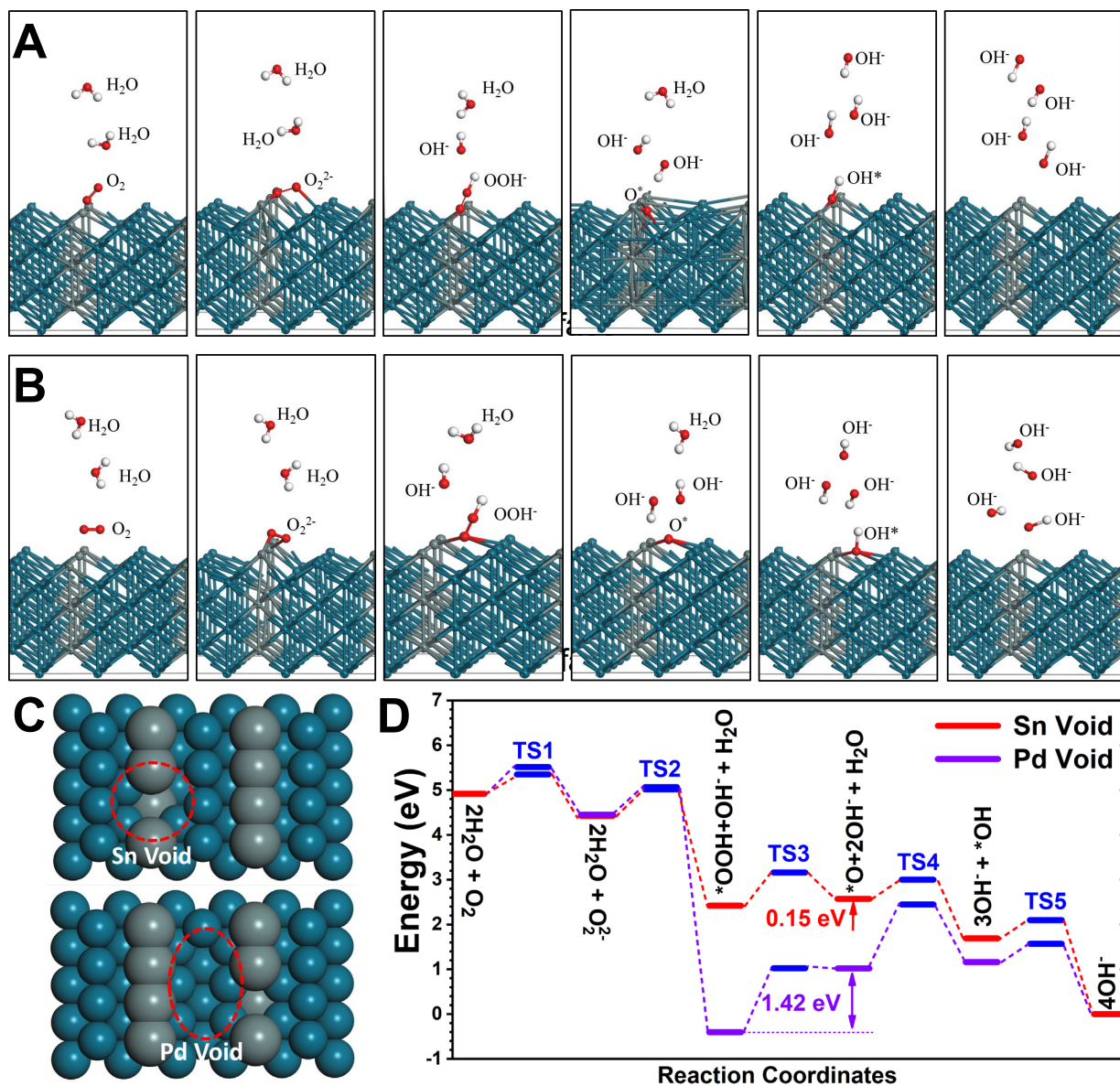


Figure 5. (A) Geometry structures of adsorption configuration with Sn defect exposure. (B) Geometry structures of adsorption configuration with Pd defect exposure. Red, white, green and grey balls represent O, H, Pd and Sn atoms, respectively. (C) Energy profile of the reaction path in ORR based on Sn defective surface configuration. (D) Energy profile of the reaction path in ORR based on Pd defective surface configuration (Pd=dark green, Sn=grey).

To further analyze the role of defects induced grain boundary of Pd₄Sn WNWs in energetics, we first created the zero misorientation surface void structures to study the different reactivity of the Sn void and

Pd void structures in alkaline ORR (**Figure 5A and 5B**). The surface defect void structures are based on creating the Schottky type defect (**Figure 5C**), which are easily formed with unique properties even without stoichiometry³⁹⁻⁴⁰. In all the optimized configurations of the process, both void structures are active in the adsorption with reactants. The reaction energy diagram (**Figure S15**) of the two paths have shown the overall energy decrease nearly -8.7 eV. Particularly, the Sn void structure shows a nearly smooth downhill route, indicating a good reactivity to the alkaline ORR. With the incorporation of the alkaline potential to the energy diagram (**Figure 5D**), the barrier height at the Pd-void route (+1.42 eV) exhibits higher than the Sn-void route (+0.15 eV). The energetic barrier encounters at the same $2e^-$ electron transfer step of forming [$*O^{2-}+2OH^-+H_2O$] for both void structures, which confirmed the dissociation of the adsorbed oxygen as the rate-determining step (RDS) in the ORR process.⁴¹ The additional calibrated energy diagrams (**Figure S16-S17**) also confirmed that the barrier of the intrinsic lattice. The Pd void show overall higher reaction energy barrier than that of Sn void, representing the higher thermodynamic and kinetic activity of Sn void region. Moreover, the more evident distortion near Sn atoms produces a stress effect after relaxation. A synergetic effect demonstrates that the surface Sn displacement induced local lattice distortion is compensated by more local relaxations from nearby Pd sites. Therefore, the zero-misorientation void structure induced by the surface defects are energetically favorable in assisting the selectivity of the ORR catalysis, especially the Sn void structure. These surface defects induced void structures have also been carefully examined for the MOR process (**Figure S18**). In comparison with the methanol poisoning route, the MOR has shown much better selectivity in energetic view. In the initial step, the MOR route (-5.65 eV) shows a nearly 4.1 times lower than the poisoning route (-1.38 eV). The MOR route also shows much fewer barriers than the poisoning route. Overall, the MOR route releases the energy of 8.23 eV, which is 4.4 times more than the poisoning route (1.87 eV). Therefore, these results have demonstrated that the high selectivity to the MOR and anti-poisoning ability is guaranteed.

The relationships between the formation of grain boundaries and surfaces defects are also investigated (**Figure S19**). In low angle grain boundaries, the formation of the surface defects induced grain boundaries are very energetically favorable as the defect concentration increases in the lattice. Especially in the high angle misorientation of grain boundaries, a slight rise in the concentration of surfaces defects significantly lowers the formation energy to the negative value, suggesting the strong strain between grains is alleviated by the defects for stabilizing the structures. Moreover, the scale of the energy decrease induced by the grain boundary is sufficient to compensate the intrinsic energy barriers at the determining step of alkaline ORR/MOR or even alter the reaction to a complete downhill trend. Therefore, the existences of grain boundaries are highly responsible for the enhancement of both ORR and MOR reactivity.

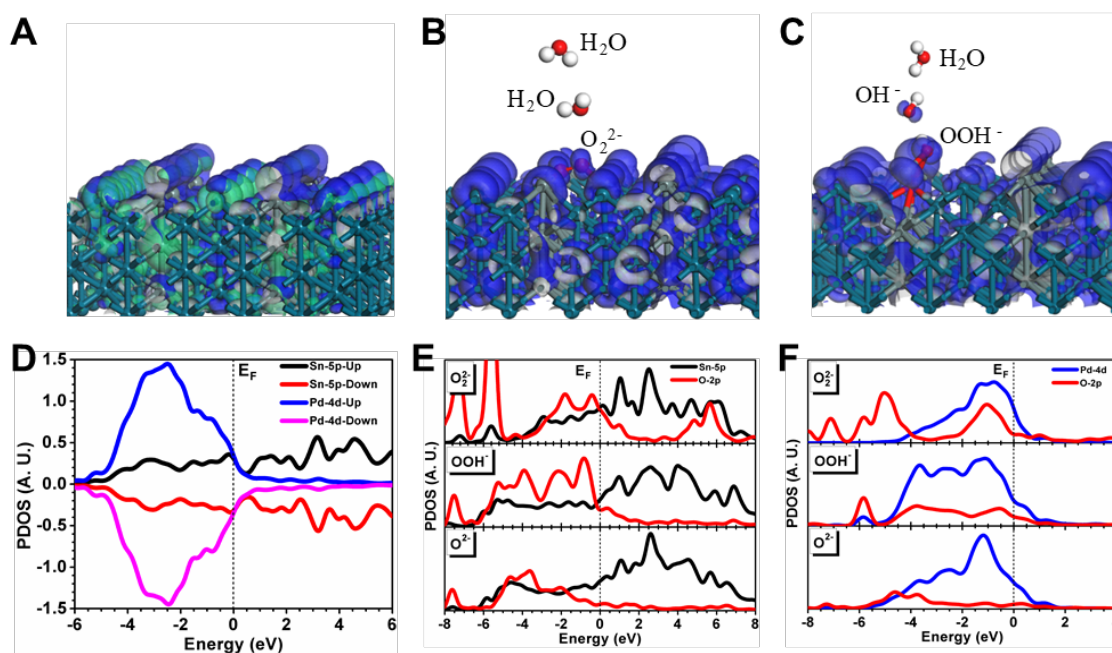


Figure 6. (A) The bonding (blue) and anti-bonding (green) orbital contour plots for the pristine Pd₄Sn surface near the E_F (Pd=dark green, Sn=grey; HOMO=blue, LUMO=green). (B) The HOMO real space contour plots for the Sn void surface with related to the initial (O_2^{2-}) adsorption. (C) The HOMO for the intermediate step of forming (OOH^-). (D) Surface PDOSs for the Pd and Sn sites. (E) The PDOSs overlap between Sn-5p and O-2p orbital at Sn defect exposure surface from the ORR reaction path. (F) The overlap between Pd-4d and O-2p orbital at Sn void surface from the ORR

reaction path.

The electronic structures regarding electronic bonding (filled-states) and anti-bonding (empty states) orbitals near the Fermi level (E_F) are further illustrated. The surface Sn-site exhibits protruded local structural configuration and shows an active electron-rich character, while the Pd-site contributes both bonding and anti-bonding orbitals since Pd-4d band center stays high and close to E_F . The high-lying electronic orbitals may further produce nearest neighboring p-d coupling yielding surface stress or folding effect induced by the surface distortions (**Figure 6A**). The HOMO distribution near E_F shows a sufficient overlapping among the O-2p, Sn-5p, and Pd-4d orbitals and demonstrates an efficient electron-transfer between catalyst surface and O-species, confirming the electroactivity of the Sn void structures (**Figure 6B** and **6C**). We reasoned the key that both Pd-4d and Sn-5p are the active orbitals responsible for the ORR catalysis. This arises because the projected partial density of states (PDOSs) reflects the Pd-4d band close to E_F with its center staying at $E_V-2.4$ eV ($E_V=0$ for E_F). Meanwhile, the pristine Sn-5p orbitals stay well matched with the Pd-4d covering range indicating a stable bonding system (**Figure 6D**). To shed more lights on the detail, the PDOSs variation trends between the two defective systems have been compared. The overlap between O-2p orbitals with the surface Pd or Sn sites is similar in the initial oxygen adsorption step, which is consistent with our discussion on the reaction energetics for both defective surfaces (**Figure 6E**). Notably, in adsorption of OOH^- , the overlap between O-2p and Sn-5p is more evident. However, in view of energy, the surface Pd-site seems to still possess natively stronger binding due to the low activation energy between Pd^0 and Pd^{2+} (**Figure 6F**). In addition, rich Pd-4d electrons transferring with O atoms results in such dramatic gain from reaction (**Figure 5D**). As the ORR reaction continues, the overlap between the surface d-band and the O-2p is weakened towards efficient desorption of OH^- in ORR. Therefore, the Sn vacancy site on the Pd_4Sn WNWs surface system is confirmed to

contribute an active barrier-minimization region. At such Sn-defect exposed region, the Sn-5p effectively tunes and redistributes the surface Pd-4d electronic activities to balance the overbinding effect. The surface Pd-sites are able to preserve the stability of the catalyst from the local distortions caused by Sn defects or protrusion defects. The Sn-5p effectively tunes and redistributes the surface Pd-4d electronic activities to balance the overbinding effect. Meanwhile, the surface Pd-sites are able to preserve the stability of the catalyst from the local distortions. Therefore, the enhanced reactivity of the Pd₄Sn WNWs is attributed to the formation of grain boundaries initiated by the surface defects.

To summarize, we have successfully developed a facile wet chemical strategy to selectively prepare 1D Pd-Sn NWs with the controllable defect (i. e. Pd₄Sn WNWs and Pd₄Sn NWs) by simply changing the synthesis solvent. Both defect-rich Pd₄Sn WNWs and penta-twinned Pd₄Sn NWs have been selectively prepared with high yields. Due to the highly abundant surface defects, the Pd₄Sn WNWs/C exhibits enhanced activity and durability toward both MOR and ORR relative to Pd₄Sn NWs/C, despite that they have similar 1D nanostructures and the same compositions, as well as commercial Pd/C and Pt/C. DFT calculations show that the surface void structures are energetically favorable in assisting both the ORR and MOR process. The further formation of misoriented grain boundaries is the key for eliminating the overall surface activation barrier to achieve excellent ORR and MOR performance. The present work highlights the importance of defect engineering in enhancing catalytic performance and provides a reference for the design of high-performance electrocatalysts as potentially practical fuel cells for energy applications in the future.

ASSOCIATED CONTENT

Supporting Information. Experimental details and data. Figures S1-19&Table S1. This material is

available free of charge *via* the Internet at <http://pubs.acs.org>.

Corresponding Author

hxq006@suda.edu.cn

Author Contributions

X.H. conceived and supervised the research. X.H. and Y.Z. designed the experiments. X.H., Y.Z., Q.S., Y.F., L.X. and Y.P. performed most of the experiments and data analysis. B.H. performed the DFT simulations. X.H. and Y.Z. wrote the paper. All authors discussed the results and commented on the manuscript. Y.Z. and B.H. contributed equally to this work.

ACKNOWLEDGMENT

This work was financially supported by Ministry of Science and Technology (2016YFA0204100, 2017YFA0208200), the National Natural Science Foundation of China (21571135, 21771156), Young Thousand Talented Program, Jiangsu Province Natural Science Fund for Distinguished Young Scholars (BK20170003), the project of scientific and technologic infrastructure of Suzhou (SZS201708), the Priority Academic Program Development of Jiangsu Higher Education Institutions (PAPD), the start-up supports from Soochow University, and the Early Career Scheme (ECS) fund (Grant No.: PolyU 253026/16P) from the Research Grant Council (RGC) in Hong Kong.

References

- (1) Gasteiger, H. A.; Markovic, N. M. *Science* **2009**, *324*, 48-49.
- (2) Wang, Y. J.; Wilkinson, D. P.; Zhang, J. J. *Chem. Rev.* **2011**, *111*, 7625-7651.
- (3) Sun, M. H.; Huang, S. Z.; Chen, L. H.; Li, Y.; Yang, X. Y.; Yuan Z. Y.; Su, B. L. *Chem. Soc. Rev.* **2016**, *45*, 3479-3563.
- (4) Xia, B. Y.; Yan, Y.; Li, N.; Wu, H. B.; Lou X. W.; Wang, X. *Nat. Energy* **2016**, *1*, 15006.

- (5) Zhu, Y. P.; Guo, C.; Zheng, Y.; Qiao, S. Z. *Acc. Chem. Res.* **2017**, *50*, 915-923.
- (6) Zou, X.; Zhang, Y. *Chem. Soc. Rev.* **2015**, *44*, 5148-5180.
- (7) Liu, H. L.; Nosheen, F.; Wang, X. *Chem. Soc. Rev.* **2015**, *44*, 3056-3078.
- (8) Kua, J.; Goddard, W. A. *J. Am. Chem. Soc.* **1999**, *121*, 10928-10941.
- (9) Xu, Y.; Zhang, B. *Chem. Soc. Rev.* **2014**, *43*, 2439-2450.
- (10) Guo, S.; Wang, E. *Nano Today* **2011**, *6*, 240-264.
- (11) Bianchini, C.; Shen, P. K. *Chem. Rev.* **2009**, *109*, 4183-4206.
- (12) Fan, Z.; Luo, Z.; Huang, X.; Li, B.; Chen, Y.; Wang, J.; Hu, Y.; Zhang, H. *J. Am. Chem. Soc.* **2016**, *138*, 1414-1419.
- (13) Guo, S.; Zhang, X.; Zhu, W.; He, K.; Su, D.; Mendoza-Garcia, A.; Ho, S. F.; Lu, G.; Sun, S. *J. Am. Chem. Soc.* **2014**, *136*, 15026-15033.
- (14) Antolini, E. *Energy Environ. Sci.* **2009**, *2*, 915-931.
- (15) Liu, M.; Lu, Y.; Chen, W. *Adv. Funct. Mater.* **2013**, *23*, 1289-1296.
- (16) Li, H. L.; Wang, L. B.; Dai, Y. Z.; Pu, Z. T.; Lao, Z. H.; Chen, Y. W.; Wang, M. L.; Zheng, X. S.; Zhu, J. F.; Zhang, W. H.; Si, R.; Ma, C.; Zeng, J. *Nat. Nanotechnol.* **2018**, *13*, 411-417.
- (17) Long, R.; Huang, H.; Li, Y. P.; Song, L.; Xiong, Y. *Adv. Mater.* **2015**, *27*, 7025-7042.
- (18) Bai, S.; Wang, C.; Deng, M.; Gong, M.; Bai, Y.; Jiang, J.; Xiong, Y. *Angew. Chem., Int. Ed.* **2014**, *53*, 12120-12124.
- (19) Tian, N.; Zhou, Z. Y.; Sun, S. G.; Ding Y.; Wang, Z. L. *Science* **2007**, *316*, 732-735.
- (20) Huang, X.; Tang, S.; Mu, X.; Dai, Y.; Chen, G.; Zhou, Z.; Ruan, F.; Yang, Z.; Zheng, N. *Nat. Nanotechnol.* **2011**, *6*, 28-32.
- (21) Chen, M.; Wu, B.; Yang, J.; Zheng, N. *Adv. Mater.* **2012**, *24*, 862-879.
- (22) Zhang, Z. C.; Xu, B.; Wang, X. *Chem. Soc. Rev.* **2014**, *43*, 7870-7886.
- (23) Ji, Y.; Luo, Y. *J. Am. Chem. Soc.* **2016**, *138*, 15896-15902.

- (24) Kuang, Q.; Lao, C.; Wang, Z. L.; Xie, Z.; Zheng, L. *J. Am. Chem. Soc.* **2007**, *129*, 6070-6071.
- (25) Lin, J.; Shang, Y.; Li, X.; Yu, J.; Wang, X.; Guo, L. *Adv. Mater.* **2017**, *29*, 1604797.
- (26) Xie, Y. P.; Yu, Z. B.; Liu, G.; Ma, X. L.; Cheng, H. M. *Energy Environ. Sci.* **2014**, *7*, 1895-1901.
- (27) Behrens, M.; Zander, S.; Kurr, P.; Jacobsen, N.; Senker, J.; Koch, G.; Ressler, T.; Fischer, R. W.; Schloegl, R. *J. Am. Chem. Soc.* **2013**, *135*, 6061-6068.
- (28) Zhang, L.; Jia, Y.; Gao, G.; Yan, X.; Chen, N.; Chen, J.; Soo, M. T.; Wood, B.; Yang, D.; Du, A.; Yao, X. *Chem.* **2018**, *4*, 287-195.
- (29) Guo, H. L.; Wang, X. F.; Qian, Q. Y.; Wang, F. B.; Xia, X. H. *ACS Nano* **2009**, *3*, 2653-2659.
- (30) Zhao, S.; Li, M.; Han, M.; Xu, D.; Yang, J.; Lin, Y.; Shi, N.-E.; Lu, Y.; Yang, R.; Liu, B.; Dai, Z.; Bao, J. *Adv. Funct. Mater.* **2018**, *28*, 1706018.
- (31) Ling, T.; Yan, D.-Y.; Jiao, Y.; Wang, H.; Zheng, Y.; Zheng, X.-L.; Mao, J.; Du, X.-W.; Hu, Z.-P.; Jaroniec, M.; Qiao, S. Z. *Nat. Commun.* **2016**, *7*, 12876.
- (32) Li, Y.; Zhou, W.; Wang, H.; Xie, L.; Liang, Y.; Wei, F.; Idrobo, J.-C.; Pennycook, S. J.; Dai, H. *Nat. Nanotechol.* **2012**, *7*, 394-400.
- (33) Yan, D.; Li, Y.; Huo, J.; Chen, R.; Dai, L.; Wang, S. *Adv. Mater.* **2017**, *29*, 1606459-1606478.
- (34) Huang, X.; Zhao, Z.; Chen, Y.; Chiu, C.-Y.; Ruan, L.; Liu, Y.; Li, M.; Duan, X.; Huang, Y. *Nano Lett.* **2014**, *14*, 3887-3894.
- (35) Li, F.; Shao, Q.; Hu, M.; Chen, Y.; Huang, X. *ACS Catal.* **2018**, *8*, 3418-3423.
- (36) Huang, X., Zheng, N. *J. Am. Chem. Soc.* **2009**, *131*, 4602-4603.
- (37) Huang, H.; Li, K.; Chen, Z.; Luo, L.; Gu, Y.; Zhang, D.; Ma, C.; Si, R.; Yang, J.; Peng, Z.; Zeng, J. *J. Am. Chem. Soc.* **2017**, *139*, 8152-8159.
- (38) Zhu, C.; Guo, S.; Dong, S. *Adv. Mater.* **2012**, *24*, 2326-2331.
- (39) Huang, B. *Inorg. Chem.* **2015**, *54*, (23), 11423-40.
- (40) Huang, B.; Sun, M.; Peng, D. *Nano Energy* **2018**, *47*, 150-171.

(41) Pei, D. N.; Gong, L.; Zhang, A. Y.; Zhang, X.; Chen, J. J.; Mu, Y.; Yu, H. Q. *Nat. Commun.* **2015**, *6*, 8696.